

# APHELION WATER-ICE CLOUD MAPPING AND PROPERTY RETRIEVAL USING THE OMEGA/MEX IMAGING SPECTROMETER.

**J.-B. Madeleine, F. Forget, A. Spiga**, *Laboratoire de Météorologie Dynamique, CNRS/UPMC/IPSL, Paris, France*, **M. Wolff**, *Space Science Institute, Boulder, Colorado, USA*, **F. Montmessin**, *LATMOS, CNRS/UVSQ/IPSL, Guyancourt, France*, **M. Vincendon, D. Jouglet, B. Gondet, J.-P. Bibring, Y. Langevin**, *Institut d'Astrophysique Spatiale, Orsay, France*, **B. Schmitt**, *Laboratoire de Planétologie de Grenoble, UJF/CNRS, France*.

Mapping of the aphelion clouds over the Tharsis plateau and retrieval of their particle size and visible opacity are made possible by the OMEGA (Observatoire pour la Minéralogie, l'Eau, les Glaces et l'Activité) imaging spectrometer aboard Mars Express. It has been difficult in the past to study the diurnal variation in cloud particle size and opacity over Tharsis due either to the sun-synchronous orbit of the spacecraft or the sparsity of observations [1, 2, 3, 4, 5, 6]. Bridging the gap, OMEGA gives an opportunity to study the diurnal variations in cloud properties thanks to the non-sun-synchronous orbit of Mars Express and to the large amount of observations made by the instrument.

We first mapped the aphelion clouds over the Tharsis plateau using the  $3.1 \mu\text{m}$  ice absorption band, and analyzed the different cloud types as a function of season and local time. Observations cover the period from MY26  $L_s = 330^\circ$  to MY29  $L_s = 180^\circ$ , and are acquired at various local times, ranging from 8 AM to 6 PM. Then, we developed an algorithm to retrieve cloud particle size and opacity. The retrieval uncertainties are satisfactory when thick clouds (opacity at  $0.67 \mu\text{m}$  nearly equal to one) are analyzed, and the method is thus applied to the thickest clouds of the Tharsis plateau. In particular, the diurnal and spatial variations in cloud particle size are analyzed, and a tentative explanation of the observed changes is given.

The results are summarized in this abstract, and details on the retrieval method, uncertainties, and observed diurnal variations will be given at the conference.

## 1 Regional mapping and cloud types

Global maps of the aphelion cloud belt in the Tharsis region are generated using the so-called cloud index. This cloud index has been first introduced by [7], and is given by the ratio of the reflectance at  $3.4 \mu\text{m}$  to that at  $3.52 \mu\text{m}$ . A sample cloud map is given in Fig. 1, in which morning hazes appear to cover the Tharsis plateau, at approximately 9 PM and for  $L_s = 30-60^\circ$ . The cloud index reflects the particle size and opacity of the clouds, and a darker shade of blue indicates an increase in these quantities.

A detailed analysis of different maps similar to the one shown in Fig. 1, and acquired at various  $L_s$  and local times, reveals four main types of clouds: morning

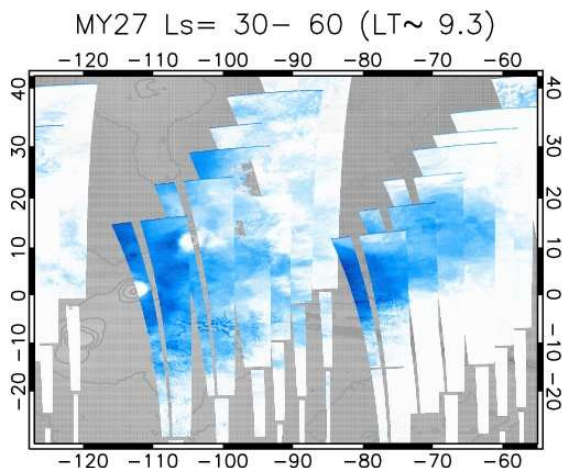


Figure 1: Cloud index map over the Tharsis plateau in mid-spring and around 9 PM, showing widespread morning hazes. Colors reflect the depth of the  $3.1 \mu\text{m}$  absorption band of water-ice. Only nadir observations are selected, and low incidence pixels ( $i > 84^\circ$ ) are removed.

hazes, topographically controlled hazes, cumulus clouds and thick hazes.

*Morning hazes* (see Fig. 1) are homogeneous and found over regions of high albedo and low thermal inertia, where the nighttime temperature is the coldest. They are probably remnants of nighttime clouds, and dissipate by noon. *Topographically controlled hazes* are thin hazes found on sloping regions at various local times, before and after the formation of the optically dense cloud belt (early spring and late summer). They might have the same origin as the well developed aphelion cloud belt, but seem to be weakened by the high temperatures and resulting difficulty to reach saturation. *Cumulus clouds* are 5 to 10 km in size, and form during early afternoon from mid spring to mid summer. These are the times when the boundary layer is the thickest, and the saturation altitude the lowest. Their time of occurrence is thus consistent with the shallow convective origin proposed by [8]. They are found especially south of Alba Patera and Valles Marineris, and coexist with thick hazes at the periphery of the cloud belt. Consequently, they might partly explain the origin of the type 1 clouds identified by [3]. *Thick hazes* are found in the afternoon, and develop

from mid spring to mid summer, especially west of the Tharsis Montes and north of Valles Marineris. They are the only clouds we can analyze in details with OMEGA, given their large optical depth. They are especially well developed around  $L_s = 100^\circ$ , as noticed by [9, 10, 11].

## 2 Cloud property retrieval

### 2.1 Retrieval method and uncertainties

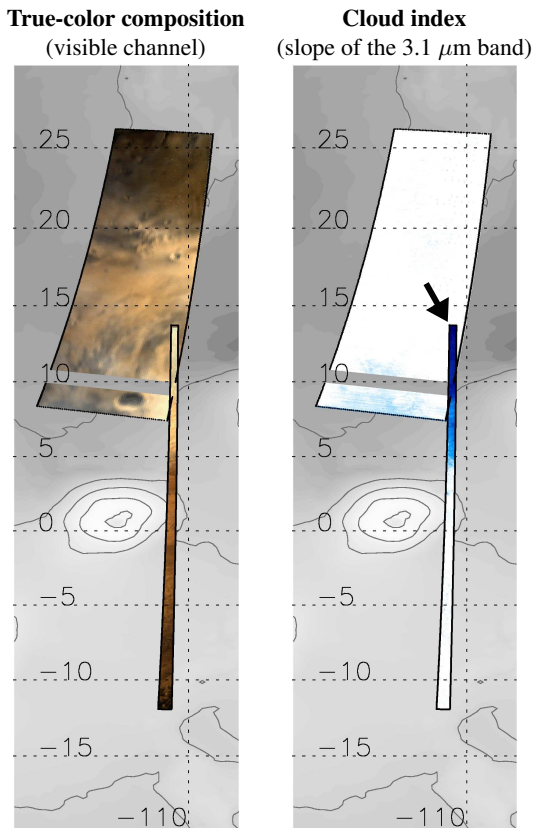


Figure 2: Sample of orbits used to retrieve cloud particle size and opacity. True-color composition (left) and cloud index (right) are represented. The wide orbit on top (3741.4) provides a cloud-free spectrum of the area pointed to by the black arrow. This is where the retrieval process is run, using the other orbit that contains thick clouds (3276.4), as indicated by the dark blue color. Shaded colors in background are MOLA topography, and Pavonis Mons is in the center.

The cloud particle size and opacity are retrieved in clouds of high optical depth, typically when the visible opacity is near unity. The same area has to be observed under cloudfree and cloudy conditions to deduce the cloud properties. The cloudfree spectrum is used to deduce the albedo of the surface, over which a synthetic cloud spectrum is fitted to the observed cloud spectrum.

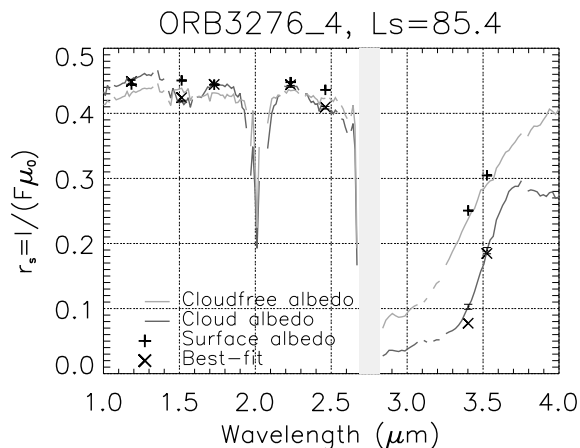


Figure 3: Typical fit obtained for the cloud shown in Fig. 2. Cloud-free spectrum is in light gray, and cloud spectrum in dark gray. The  $1.5 \mu\text{m}$  water ice absorption band is clearly seen, whereas the  $2$  and  $3.1 \mu\text{m}$  bands are reflected by the negative and positive slopes around  $2.2$  and  $3.4 \mu\text{m}$ , respectively. + crosses show the surface albedo obtained after removing the contributions of scattering by the dust layer and thermal emissions. x crosses represent the final best-fit. Instrumental  $1-\sigma$  error is also given for the cloud spectrum, but can hardly be distinguished, except maybe in the L channel.

A retrieval example is shown in Fig. 2, in which the cloudfree (upper left) and cloudy (lower right) orbits are represented. The arrow indicates where the two retrieval spectra are located, the latter being shown in Fig. 3. The retrieval is done by removing the contribution of atmospheric dust, using the dust opacity measurements made simultaneously by the MERs [12, 13], and by accounting for thermal emissions, using the temperatures of the Mars Climate Database v4.3 [14, 15].

Extrapolating the measurements from the rovers introduces a large error on the dust content of the atmosphere, which results in an uncertainty on surface albedo. The impact of the uncertainty on surface albedo grows with decreasing cloud opacity, explaining why our method is limited to high opacity clouds. This uncertainty is the main source of error in our retrieval. The other main uncertainties are surface temperature and instrumental error.

The overall relative error on the retrieved parameters is less than 30% for  $r_{\text{eff,ice}}$ , and 20% for  $\tau_{\text{ice}}$ . A systematic bias toward ice particle sizes which are at most 20-30% too small is also possible, due to the change in ice optical indices as a function of cloud temperature.

### 2.2 Retrieved properties

The effective radius,  $0.67 \mu\text{m}$  opacity and water ice content (WIC) are retrieved in the densest parts of the cloud belt. The locations of the different retrievals are given

in Fig. 4, and the corresponding results are listed in Table 1. The WIC in  $\text{pr.}\mu\text{m}$  is deduced from the cloud particle size and opacity using the following equation:

$$\text{WIC} = \int_0^\infty N \frac{4}{3} \pi r^3 n(r) dr = \frac{4}{3} N r_{\text{eff}} \sigma_g = \frac{4}{3} \frac{\tau r_{\text{eff}}}{Q_{\text{ext}}}, \quad (1)$$

where  $n(r)$  is a lognormal distribution ( $\nu_{\text{eff}} = 0.1$ ),  $r_{\text{eff}}$  the effective radius of the distribution in  $\mu\text{m}$ , and where  $Q_{\text{ext}}$  varies as a function of the ice particle size. The error on the WIC is directly deduced from the errors on  $r_{\text{eff,ice}}$  and  $\tau_{\text{ice}}$ . Ice particle sizes are consistent with previous analyses, range from 2.2 to 5.4  $\mu\text{m}$ , and belong to type 2 clouds reported by [3]. The WIC can be considered as maximal, since we focus on the densest part of the cloud belt, and is equal to 1.3-5.2  $\text{pr.}\mu\text{m}$ .

Particle sizes can be separated in two groups, of 2-3.5 and 5  $\mu\text{m}$ , respectively. These two groups do not correspond to different  $L_s$  or local times, and their presence probably result from regional changes of the meteorological conditions. The first group (retrievals # 7, 9, 10, 11 and 12 of Fig. 4) may represent the ‘‘background’’ hazes found in the cloud belt, whereas the second group (other retrievals of Fig. 4) may correspond to regions of enhanced cloud formation. Particle sizes of the second group appear to be quite constant over  $L_s$  and local time, and always close to 5  $\mu\text{m}$ . The second group is found mostly west of Ascraeus and Pavonis Mons, and also west of Lunae Planum. These are regions of strong anabatic winds, and these large particles could be created in environments that are strongly controlled by local dynamics and topography. A good example is provided by the Tharsis volcanoes, described by [16] as ‘‘water pumps’’ where large particles forms locally before being carried westward by the regional circulation. This kind of formation processes, enhanced by the local wind dynamics, would explain why these particles are larger than the others. It would also account for their quite constant size over time, since they would rapidly grow to reach a threshold size and leave their formation environment.

### 3 Perspectives

The aphelion clouds display various morphologies and microphysical properties, and a lot is still to be learned about their formation processes and environments. The method described here could be applied to other regions, as long as ice is not present on the surface. The same kind of approach could also be used with CRISM/MRO, and coupled to its ability to acquire multi-angle data. It would probably allow the extension of this analysis to thinner clouds (such as cumulus clouds) and improve our understanding of aphelion cloud formation.

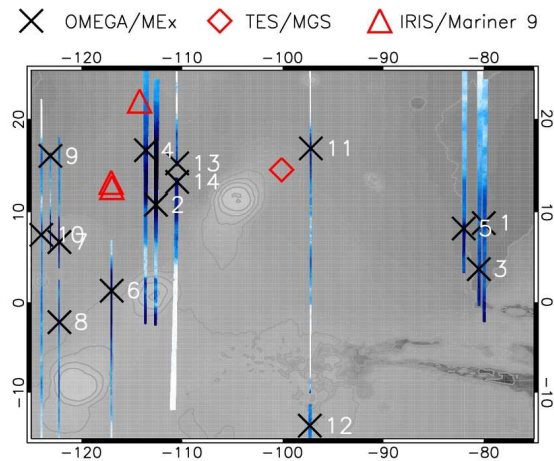


Figure 4: Map showing the location of the cloud property retrievals, which are listed in Table 1. Also represented in red are IRIS and TES retrievals, that have been published by [17] and [4], respectively. The cloud index map corresponding to each retrieval is also shown. A focus is made on the peak of the cloud season, around  $100^\circ$  of  $L_s$ . Solar longitude thus ranges from  $L_s = 85.4^\circ$  to  $L_s = 121.4^\circ$ .

### References

- [1] R. J. Curran, B. J. Conrath, R. A. Hanel, V. G. Kunde, and J. C. Pearl, ‘‘Mars: Mariner 9 Spectroscopic Evidence for  $\text{H}_2\text{O}$  Ice Clouds,’’ *Science*, vol. 182, pp. 381–383, Oct. 1973.
- [2] E. Petrova, H. U. Keller, W. J. Markiewicz, N. Thomas, and M. W. Wuttke, ‘‘Ice hazes and clouds in the Martian atmosphere as derived from the Phobos/KRFM data,’’ *Planetary and Space Science*, vol. 44, pp. 1163–1176, Oct. 1996.
- [3] R. T. Clancy, M. J. Wolff, and P. R. Christensen, ‘‘Mars aerosol studies with the MGS TES emission phase function observations: Optical depths, particle sizes, and ice cloud types versus latitude and solar longitude,’’ *Journal of Geophysical Research (Planets)*, vol. 108, pp. 2–1, Sept. 2003.
- [4] M. Wolff and R. Clancy, ‘‘Constraints on the size of Martian aerosols from Thermal Emission Spectrometer observations,’’ *Journal of Geophysical Research*, vol. 108, no. E9, p. 5097, 2003.
- [5] L. K. Tamppari, R. W. Zurek, and D. A. Paige, ‘‘Viking-era diurnal water-ice clouds,’’ *Journal of Geophysical Research (Planets)*, vol. 108, pp. 5073–+, July 2003.
- [6] D. A. Glenar, R. E. Samuelson, J. C. Pearl, G. L. Bjoraker, and D. Blaney, ‘‘Spectral imaging of martian water ice clouds and their diurnal behavior during the 1999 aphelion season ( $L_s = 130^\circ$ ),’’ *Icarus*, vol. 161, pp. 297–318, Feb. 2003.

OMEGA analysis of Mars water ice clouds

#	orbit	lon (°)	lat (°)	$L_s$ (°)	LT (h)	$z$ (km)	$i$ (°)	$e$ (°)	$r_{\text{eff},i}$ ( $\mu\text{m}$ )	$\sigma_{r_{\text{eff},i}}$ ( $\mu\text{m}$ )	$\tau_i$	$\sigma_{\tau_i}$	WIC (pr. $\mu\text{m}$ )	$\sigma_{\text{WIC}}$ (pr. $\mu\text{m}$ )
1	0887_5	-80.0	8.8	93.3	16.9	-0.6	69.9	5.7	5.4	+1.1 -0.8	1.0	+0.12 -0.12	3.3	+0.9 -1.1
2	0891_5	-112.6	10.8	93.8	16.5	2.5	68.8	2.5	5.0	+0.4 -0.3	1.7	+0.09 -0.09	5.2	+0.6 -0.6
3	0898_5	-80.5	3.7	94.7	15.8	-0.8	71.2	2.3	4.7	+0.5 -0.4	1.3	+0.09 -0.10	3.7	+0.6 -0.6
4	0902_5	-113.6	16.7	95.2	15.6	2.2	64.6	2.7	4.9	+0.7 -0.5	1.2	+0.10 -0.11	3.6	+0.7 -0.8
5	0920_5	-82.0	8.2	97.4	16.4	0.0	66.3	1.5	4.7	+0.7 -0.5	1.2	+0.10 -0.11	3.5	+0.7 -0.8
6	0946_6	-117.0	1.3	100.7	15.6	5.2	65.7	0.4	4.7	+1.3 -0.8	0.8	+0.13 -0.13	2.3	+0.8 -1.0
7	1012_6	-122.2	6.7	109.1	14.8	4.5	53.4	0.3	3.4	+0.4 -0.3	1.4	+0.10 -0.10	2.9	+0.5 -0.5
8	1012_7	-122.2	-2.2	109.1	14.8	5.0	58.0	0.3	5.1	+1.8 -1.2	0.7	+0.15 -0.11	2.2	+0.9 -1.2
9	1023_6	-123.1	16.1	110.5	15.6	1.0	47.8	0.1	2.3	+0.6 -0.4	1.0	+0.18 -0.19	1.3	+0.5 -0.6
10	1034_6	-124.0	7.5	111.9	15.4	4.6	49.8	0.2	2.2	+0.3 -0.2	1.3	+0.12 -0.13	1.7	+0.4 -0.4
11	1107_1	-97.2	16.9	121.4	13.5	2.6	35.2	0.1	2.8	+0.3 -0.3	1.4	+0.10 -0.11	2.3	+0.4 -0.5
12	1107_2	-97.3	-13.6	121.4	13.7	6.6	51.9	0.3	2.4	+0.4 -0.3	1.2	+0.12 -0.13	1.7	+0.4 -0.5
13	3276_3	-110.5	15.3	85.4	14.2	2.0	29.9	0.4	4.8	+0.7 -0.5	1.1	+0.11 -0.11	3.3	+0.7 -0.8
14	3276_4	-110.5	13.3	85.4	14.4	2.0	30.9	0.3	3.9	+0.3 -0.3	1.5	+0.09 -0.09	3.5	+0.5 -0.5

Table 1: List of all the retrievals performed over the Tharsis plateau (see the map of Fig. 4) for the  $L_s = 85.4\text{--}121.4^\circ$  period. The altitude of the surface above the areoid and the observing geometry are given for each observation. Measured ice particle size and cloud visible opacity are listed, along with the Water Ice Column in pr. $\mu\text{m}$  (WIC). Corresponding 1- $\sigma$  errors are also given.

- [7] Y. Langevin, J. Bibring, F. Montmessin, F. Forget, M. Vincendon, S. Douté, F. Poulet, and B. Gondet, “Observations of the south seasonal cap of Mars during recession in 2004–2006 by the OMEGA visible/near-infrared imaging spectrometer on board Mars Express,” *Journal of Geophysical Research (Planets)*, vol. 112, pp. 8–+, July 2007.
- [8] I. T. Michaels and C. R. Rafkin Scot, “Large-eddy simulation of atmospheric convection on Mars,” *Quarterly Journal of the Royal Meteorological Society*, vol. 130, pp. 1251–1274, Apr. 2004.
- [9] J. L. Benson, B. P. Bonev, P. B. James, K. J. Shan, B. A. Cantor, and M. A. Caplinger, “The seasonal behavior of water ice clouds in the Tharsis and Valles Marineris regions of Mars: Mars Orbiter Camera Observations,” *Icarus*, vol. 165, pp. 34–52, Sept. 2003.
- [10] M. D. Smith, “Interannual variability in TES atmospheric observations of Mars during 1999–2003,” *Icarus*, vol. 167, pp. 148–165, Jan. 2004.
- [11] N. Mateshvili, D. Fussen, F. Vanhellemont, C. Bingen, J. Dodion, F. Montmessin, S. Perrier, E. Dimarellis, and J. Bertaux, “Martian ice cloud distribution obtained from SPICAM nadir UV measurements,” *Journal of Geophysical Research (Planets)*, vol. 112, pp. 7004–+, July 2007.
- [12] M. T. Lemmon, M. J. Wolff, M. D. Smith, R. T. Clancy, D. Banfield, G. A. Landis, A. Ghosh, P. H. Smith, N. Spanovich, B. Whitney, P. Whelley, R. Greeley, S. Thompson, J. F. Bell, and S. W. Squyres, “Atmospheric Imaging Results from the Mars Exploration Rovers: Spirit and Opportunity,” *Science*, vol. 306, pp. 1753–1756, Dec. 2004.
- [13] M. Vincendon, Y. Langevin, F. Poulet, A. Pommerol, M. Wolff, J.-P. Bibring, B. Gondet, and D. Jouglet, “Yearly and seasonal variations of low albedo surfaces on Mars in the OMEGA/MEx dataset: Constraints on aerosols properties and dust deposits,” *Icarus*, vol. 200, pp. 395–405, Apr. 2009.
- [14] F. Forget, F. Hourdin, R. Fournier, C. Hourdin, O. Talagrand, M. Collins, S. R. Lewis, P. L. Read, and J.-P. Huot, “Improved general circulation models of the Martian atmosphere from the surface to above 80 km,” *Journal of Geophysical Research*, vol. 104, pp. 24155–24176, Oct. 1999.
- [15] E. Millour, F. Forget, F. González-Galindo, A. Spiga, S. Lebonnois, L. Montabone, S. R. Lewis, P. L. Read, M. A. López-Valverde, G. Gilli, F. Lefèvre, F. Montmessin, M. Desjean, J. Huot, and The McD/Gcm Development Team, “The Latest (Version 4.3) Mars Climate Database,” *LPI Contributions*, vol. 1447, pp. 9029–+, Nov. 2008.
- [16] T. I. Michaels, A. Colaprete, and S. C. R. Rafkin, “Significant vertical water transport by mountain-induced circulations on Mars,” *Geophysical Research Letters*, vol. 33, pp. 16201–+, Aug. 2006.
- [17] L. Zasova, D. Grassi, V. Formisano, and A. Maturilli, “The Martian atmosphere in the region of the great volcanoes: Mariner 9 IRIS data revisited,” *Planetary and Space Science*, vol. 49, pp. 977–992, Aug. 2001.